We are IntechOpen,
the world's leading publisher of
Open Access books
Built by scientists, for scientists

4,800
Open access books available

122,000
International authors and editors

135M
Downloads

Our authors are among the

154
Countries delivered to

TOP 1%
most cited scientists

12.2%
Contributors from top 500 universities

CLARIVATE ANALYTICS
BOOK CITATION INDEX
INDEXED

WEB OF SCIENCE™

Selection of our books indexed in the Book Citation Index
in Web of Science™ Core Collection (BKCI)

Interested in publishing with us?
Contact book.department@intechopen.com

Numbers displayed above are based on latest data collected.
For more information visit www.intechopen.com

Nano-metrology based on the Laser Interferometers

Saeed Olyaee and Samaneh Hamedi
Nano-Photonics and Optoelectronics Research Laboratory
Shahid Rajaee Teacher Training University
Iran

1. Introduction

In recent years, demands for non-contact displacement measurement systems with sub-nanometer uncertainty have significantly increased. One technique to reach the non-contact displacement measurements is based on the use of interferometers. Since 1887 when Michelson and Morley did the famous experiment to detect possible changes in the speed of light in different directions, optical interferometry has been widely used in length-related measurements (Wu et al., 2002). Low-coherence interferometry (LCI) is an optical technique that may be used for industrial surface metrology with accuracy in the micron range. Displacement measurement systems based on the coherent methods provide a high accuracy measurement in different axes. The laser interferometers can measure the absolute positions as well as displacements in a wide dynamic range by measuring the changes of laser interference fringes.

A high precision displacement measurement is necessary in many applications such as photolithography, transducer calibration, geodesy, semiconductor fabrication, precision cutting, shape measurement, and robotic systems. The fabrication of semiconductor chips requires lithographic stepper machines in order to measure high accuracy displacement (Brink et al., 1996; Demarest, 1998). The planar lithographic fabrication process is used to fabricate many nano-systems like electronic, photonic, magnetic, mechanical, chemical, and biological devices. Semiconductor manufacturing tools depend on accurate metrology frames such as lithography scanners and steppers, lithography mask (reticle) writers, circuit and mask repair tools, CD metrology tools, pattern placement, and overlay metrology tools. Pattern placement metrology measures and/or controls pattern location and overlay. A metrology frame consists of three components stable structure, length scale (e.g., wavelength of light), and means to compare work piece with length scale (e.g., microscope).

The minimum feature of the integrated circuits can be decreased by improvement in accuracy in the displacement measurements. The most important requirements for future photolithography and masking process such as accuracy of nano-displacement are annually reported by ITRS (ITRS, 2008). Industrial development of semiconductor devices and circuits is asking for improved resolution and reached the high accuracy of nano-metrology systems.

The laser interferometers are mainly divided into two categories; homodyne and heterodyne. The laser heterodyne interferometers have been widely used in displacement measuring systems with sub-nanometer resolution. During the last few years nanotechnology has been changed from a technology only applied in semiconductor industry to the invention of new production with micro and nanometer size until in future picometer size such as, nano electro mechanical systems (NEMS), semiconductor nano-systems, nano-sensors, nano-electronics, nano-photonics and nano-magnetics (Schattenburg & Smith, 2001).

In this chapter, we investigate some laser interferometers used in the nano-metrology systems, including homodyne interferometer, two-longitudinal-mode laser heterodyne interferometer, and three-longitudinal-mode laser heterodyne interferometer (TLMI). Throughout the chapter, we use the notations described in Table 1.

2. Principles of the Laser Interferometers as Nano-metrology System

2.1 Interference Phenomenon

Everyone has seen interference phenomena in a wet road, soap bubble and like this. Boyle and Hooke first described interference in the 17th century. It was the start point of optical interferometry, although the development of optical interferometry was stop because the theory of wave optics was not accepted.

A beam of light is an electromagnetic wave. If we have coherence lights, interference phenomenon can be described by linearly polarized waves. The electrical field E in z direction is represented by exponential function as (Hariharan, 2003):

$$E = \text{Re}\{a\exp[i2\pi\nu(t - z/c)]\} \tag{1}$$

where a is the amplitude, t is the time, ν is the frequency of the light source and c is the speed of propagation of the wave. If all equations on E are linearly assumed, it can be renewed as:

$$\begin{aligned} E &= \text{Re}\{a\exp(-i2\pi\nu\,z/c)\exp(i2\pi\nu\,t)\} \\ &= \text{Re}\{a\exp(-i\varphi)\exp(i2\pi\nu\,t)\} \end{aligned} \tag{2}$$

The real part of this equation is:

$$E = A\exp(i2\pi\nu t) \tag{3}$$
$$A = a\exp(-i\varphi)$$

where

$$\varphi = \frac{2\pi\nu\,z}{c} = \frac{2\pi n z}{\lambda} \tag{4}$$

In this formula λ is the wavelength of light and n is the refractive index of medium. According to Fig. 1, if two monochromic waves with the same polarization propagate in the same direction, the total electric field at the point P is given by:

$$E = E_1 + E_2 \tag{5}$$

where E_1 and E_2 are the electric fields of two waves. If they have the same frequency, the total intensity is then calculated as:

$$I = \left| A_1 + A_2 \right|^2 \tag{6}$$

| Abbreviations		Constants & Symbols	
APD	avalanche photodiode	$\widetilde{E}$	amplitude of leakage electrical field
BPF	Band pass filter	$\hat{E}$	amplitude of main electrical field
BS	non-polarizing beam splitter	f_s	secondary beat frequency
CCP	corner cube prism	$f_{bH} = \nu_3 - \nu_2$	higher intermode beat frequency
DBM	double-balanced mixer	$f_{bL} = \nu_2 - \nu_1$	the lower intermode beat frequency
FP	frequency-path	I_b	base photocurrent
IVC	I to V converter	I_m	measurement photocurrent
LCI	low-coherence interferometry	n	refractive index of medium
LP	linear polarizer	$\overline{V}$	target velocity
OPD	optical path difference	α	rotation angle of the PBS with respect to the laser polarization axis
PBS	polarizing-beam splitter	α and β	non-orthogonality of the polarized beams
TLMI	three-longitudinal-mode interferometer	δ_{ε_t} and δ_{ε_r}	ellipticity of the central and side modes
Vectors & Jones Matrices		Δf	Doppler shift
LP	matrix of LP	Δz	the displacement measurement
RCCP	matrix of reference CCP	$\Delta \varphi$	the phase change
RPBS	matrix of reference PBS	$\Delta \Phi$	the phase change resulting from optical path difference
TCCP	matrix of target CCP	φ_0	the initial phase corresponding to the electrical field of E_i
TPBS	matrix of target PBS	λ	the wavelength of input source
$\vec{\mathbf{E}}_{\mathbf{LP}_X}$	X component of the total electric field	Λ_{II}	the synthetic wavelength in two-mode laser heterodyne interferometer
$\vec{\mathbf{E}}_{\mathbf{LP}_y}$	Y component of the total electric field	Λ_{III}	the synthetic wavelength in three-mode laser heterodyne interferometer
Constants & Symbols		ν	the optical frequency
c	the speed of light in vacuum	θ	the deviation angle of polarizer referred to $45°$
$d\varepsilon$	ellipticity of the polarized beams	ρ	the reflection coefficients of the PBS
$\vec{E}$	electrical field vector	ω	optical angular frequency
ℓ	the number of distinct interference terms	τ	the transmission coefficients of the PBS
ψ	nonlinearity phase	$\aleph$	the number of active FP elements

Table 1. Nomenclatures
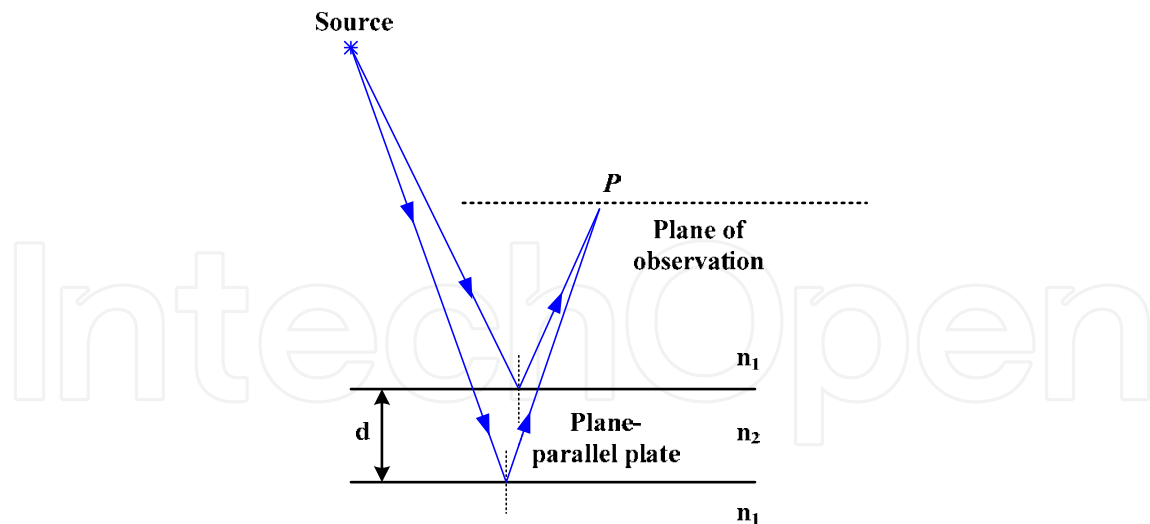
Fig. 1. Formation of interference in a parallel plate waves

$$I = A_1^2 + A_2^2 + A_1 A_2^* + A_1^* A_2$$
$$= I_1 + I_2 + 2(I_1 I_2)^{1/2} \cos \Delta\varphi \tag{7}$$

where I_1 and I_2 are the intensities at point P, resulting from two waves reflected by surface and

$$A_1 = a_1 \exp(-i\varphi_1) \tag{8}$$
$$A_2 = a_2 \exp(-i\varphi_2) \tag{9}$$

The phase difference between two waves at point P is given by:

$$\Delta\varphi = \varphi_1 - \varphi_2 = \frac{2\pi v \Delta z}{c} = \frac{2\pi n \Delta z}{\lambda} \tag{10}$$

According to Eq. (10), the displacement can be calculated by detecting the phase from interference signal. An instrument which is used to measure the displacement based on the interferometry phenomenon is interferometer. Michelson has presented the basic principals of optical displacement measurement based on interferometer in 1881. According to using a stabilized He-Ne as input source (Yokoyama et al., 1994; Eom et al., 2002; Kim & Kim, 2002; Huang et al., 2000; Yeom & Yoon, 2005), they are named laser interferometers. Two kinds of laser interferometers depending on their detection principles, homodyne or heterodyne methods, have been developed and improved for various applications.

Homodyne interferometers work due to counting the number of fringes. A fringe is a full cycle of light intensity variation, going from light to dark to light. But the heterodyne interferometers work based on frequency detecting method that the displacement is arrived from the phase of the beat signal of the interfering two reflected beams. On the other hand, heterodyne method such as Doppler-interferometry in comparison with homodyne method provides more signal-to-noise ratio and easier alignment in the industrial field applications (Brink et al., 1996). Furthermore, the heterodyne interferometers are known to be immune to environmental effects. Two-frequency laser interferometers are being widely used as useful instruments for nano-metrology systems.

2.2 Homodyne Interferometer

Commercial homodyne laser interferometers mainly includes a stabilized single frequency laser source, two corner cube prisms (CCPs), a non-polarizing beam splitter (BS), two avalanche photodiodes (APDs), and measurement electronic circuits. The laser frequency stabilization is many important to measure the displacement accurately. A laser source used in the interferometers is typically a He-Ne laser.

An improved configuration of the single frequency Michelson interferometer with phase quadrature fringe detection is outlined in Fig. 2. A 45° linearly polarized laser beam is split by the beam splitter. One of the two beams, with linear polarization is reflected by a CCP_r which is fixed on a moving stage. The other beam passes through a retarder twice, and consequently, its polarization state is changed from linear to circular. The electronics following photodetectors at the end of interferometer count the fringes of the interference signal (see section 3.2). With interference of beams, two photocurrent signals I_x and I_y are concluded as:

$$I_y = a \sin\left(\frac{4n\pi}{\lambda}\Delta z\right) \tag{11}$$

$$I_x = b \cos\left(\frac{4n\pi}{\lambda}\Delta z\right) \tag{12}$$

where Δz is the displacement of CCP_t which is given by:

$$\Delta z = \frac{\lambda}{4n\pi}\tan^{-1}\left(\frac{I_y}{I_x}\right) \tag{13}$$

This is called a DC interferometer, because there is no dependency to the time in the measurement signal (Cosijns, 2004).

2.3 Heterodyne Interferometer

A heterodyne laser interferometer contains a light source of two- or three-longitudinal-mode with orthogonal polarizations, typically a stabilized multi-longitudinal-mode He-Ne laser. The basic setup of a two-mode heterodyne interferometer is shown in Fig. 3. The electric field vectors of laser source are represented by:

$$\vec{E}_1 = \hat{E}_{01}\exp(2\pi\nu_1 t + \varphi_{01})\vec{e}_1 \tag{14}$$

$$\vec{E}_2 = \hat{E}_{02}\exp(2\pi\nu_2 t + \varphi_{02})\vec{e}_2 \tag{15}$$

where $\hat{E}_{01}$ and $\hat{E}_{02}$ are the electric field amplitudes, ν_1 and ν_2 are the optical frequencies stabilized in the gain profile and φ_{01} and φ_{02} represent the initial phases. As it can be seen from Fig. 3, the optical head consists of the base and measurement arms. The laser output beam is separated by a non-polarizing beam splitter from which the base and measurement beams are produced. The base beam passing through a linear polarizer is detected by a

photodetector. Consequently, in accordance with Eq. (6), the base photocurrent I_b with $v_2 - v_1$ intermode beat frequency is obtained as:

$$I_b = 2\hat{E}_{01}\hat{E}_{02}\cos\left(2\pi(v_2 - v_1)t + (\phi_{02} - \phi_{01})\right) \tag{16}$$
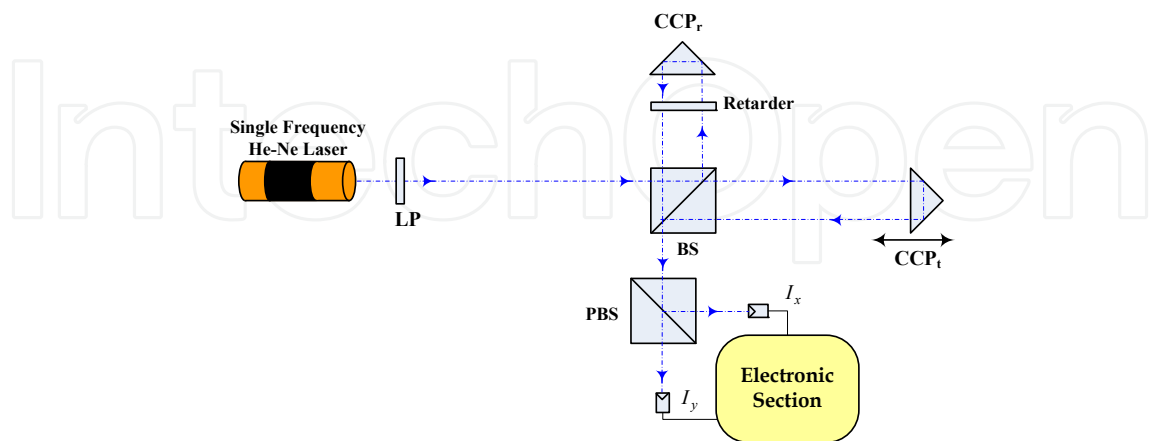

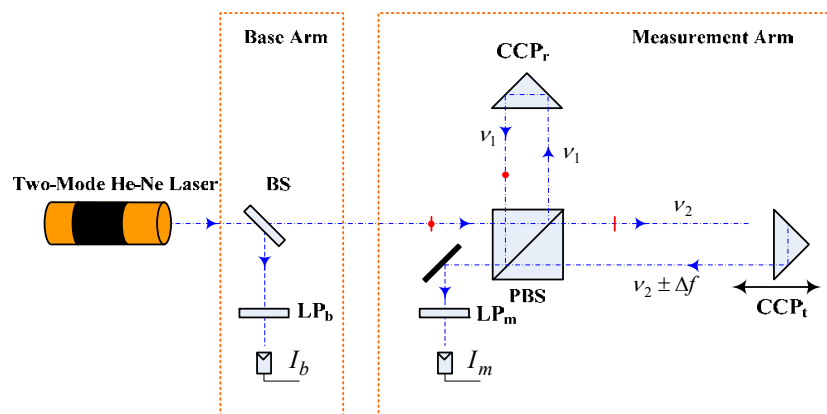Fig. 2. The schematic representation of homodyne laser interferometer

Fig. 3. The schematic representation of heterodyne laser interferometer

As it is concluded from Eq. (16), the heterodyne interferometer works with the frequency ($v_2 - v_1$), therefore it is called an AC interferometer. The measurement beam is split into two beams namely target and reference beams by the polarizing-beam splitter (PBS) and are directed to the corner cube prisms. The phases of modes are shifted in accordance with the optical path difference (OPD). To enable interference, the beams are transmitted through a linear polarizer (LP) under 45° with their polarization axes. After the polarizer, a photodetector makes measurement signal I_m :

$$I_m = 2\hat{E}_{01}\hat{E}_{02}\cos\left(2\pi(v_2 - v_1)t + (\varphi_{02} - \varphi_{01}) + (\varphi_t - \varphi_r)\right) \tag{17}$$

The phase difference between base and measurement arms represents the optical path difference which is dependent to the displacement measurement. As the CCP_t in the measurement arm moves with velocity $\overline{V}$, a Doppler shift is generated for v_2 :

$$\Delta f = 2\pi \left(\frac{2n\overline{V}\nu_2}{c} \right) \tag{18}$$

The phase change in the interference pattern is dependent on the Doppler frequency shift:

$$\Delta\Phi = \int\limits_{t_1}^{t_2} 2\pi\Delta\nu\, t = \frac{4n\pi\nu_2}{c}\Delta z \tag{19}$$

Finally, the displacement measurement of the target with vacuum wavelength λ_2 is given as:

$$\Delta z = \frac{\Delta\Phi\lambda_2}{4n\pi} \tag{20}$$

3. Comparison Study between Two- and Three-Longitudinal-Mode Laser Heterodyne Interferometers

3.1 The Optical Head

To reach higher resolution and accuracy in the nanometric displacement measurements, a stabilized three-longitudinal-mode laser can replace two-longitudinal-mode laser. In the two-mode interferometer, one intermode beat frequency is produced, whereas in three-mode interferometer three primary beat frequencies and a secondary beat frequency appear. Although the three-longitudinal-mode interferometers (TLMI) have a higher resolution compared to two-longitudinal-mode type, the maximum measurable velocity is dramatically reduced due to the beat frequency reduction. Yokoyama et al. designed a three-longitudinal-mode interferometer with 0.044 nm resolution, assuming the phase detection resolution of 0.1° (Yoloyama et al., 2001). However, limitation of the velocity in the displacement measurement can be eliminated by a proper design (Yokoyama et al., 2005).

The source of the multiple-wavelength interferometer should produce an appropriate emission spectrum including of several discrete and stabilized wavelengths. The optical frequency differences determine the range of non-ambiguity of distance and the maximum measureable velocity. The coherence length of the source limits the maximal absolute distance, which can be measured by multiple-wavelength. If we consider a two-wavelength interferometry using the optical wavelengths λ_1 and λ_2 with orthogonal polarization, the phase shift of each wavelength will be:

$$\Phi_i = \frac{4\pi\Delta z}{\lambda_i} \tag{21}$$

where Δz is the optical path difference and Φ_i is the phase shift corresponding to the wavelength λ_i. Therefore, the phase difference between λ_1 and λ_2 is given by:

$$\Delta\Phi = 4\pi\Delta z \left(\frac{1}{\lambda_1} - \frac{1}{\lambda_2} \right) \tag{22}$$

And the synthetic wavelength, Λ_{II}, can be expressed as:

$$\Lambda_{\mathrm{II}} = \frac{\lambda_1 \lambda_2}{|\lambda_1 - \lambda_2|} = \frac{c}{|v_1 - v_2|} \tag{23}$$

where v_1 and v_2 are the optical frequencies corresponding to λ_1 and λ_2, and c is the speed of light in vacuum. If the number of stabilized wavelengths in the gain curve increase to three-longitudinal-mode, the synthetic wavelength is obtained as:

$$\Lambda_{\mathrm{II}} = \frac{\lambda_1 \lambda_2 \lambda_3}{|\lambda_1 \lambda_2 - 2\lambda_1 \lambda_3 + \lambda_2 \lambda_3|} = \frac{c}{f_s} \tag{24}$$

where f_s is the secondary beat frequency in the three-mode laser heterodyne interferometers. Therefore, the synthetic wavelength in the three-longitudinal-mode interferometer comparing to two-mode system is considerably increased (Olyaee & Nejad, 2007c). The stabilized modes in the gain profile of the laser source and optical head of the nano-metrology system on the basis of two- and three-longitudinal-mode lasers are shown in Fig. 4. As it is represented three wavelengths for which the polarization of the side modes λ_1 and λ_3 is orthogonal to the polarization of the central mode λ_2. The electric field of three modes of laser source is obtained as:

$$E_i = \hat{E}_i \sin(2\pi v_i t + \varphi_i) \quad , \quad i = 1,2,3 \tag{25}$$

where φ_i is the initial phases corresponding to the electric field E_i. In both cases, the optical head consists of the base and measurement arms. First, the laser output is separated by BS, so that base and measurement beams are produced. Then, the beam is split into two subsequent beams by PBS and directed to each path of the interferometers. Two reflected beams are interfered to each other on the linear polarizer. Because of orthogonally polarized modes, the linear polarizer should be used to interfere two beams as shown in Fig. 5. The stabilized multimode He-Ne lasers are chosen in which the side modes can be separated from the center mode due to the orthogonal polarization states.

But in reality, non-orthogonal and elliptical polarizations of beams cause each path to contain a fraction of the laser beam belonging to the other path. Hence, the cross-polarization error is produced. In the reference path (path.1) of TLMI, v_1 and v_3 are the main frequencies and v_2 is the leakage one, whereas in the target path (path.2), v_2 is the main signal and the others are as the leakages.
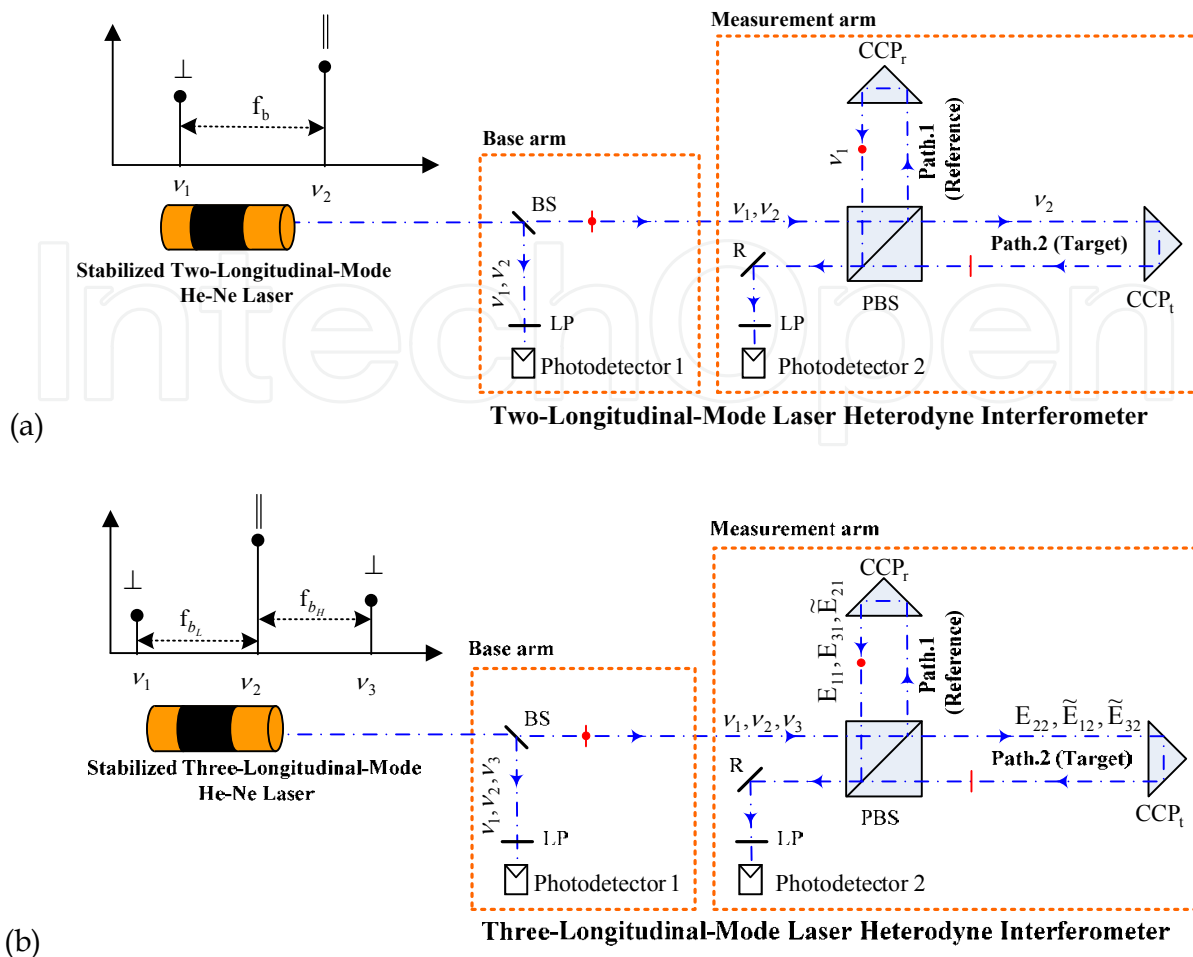
Fig. 4. The stabilized modes in gain profile and optical head of the nano-metrology system based on (a) the two- and (b) three-longitudinal-mode He-Ne laser interferometers
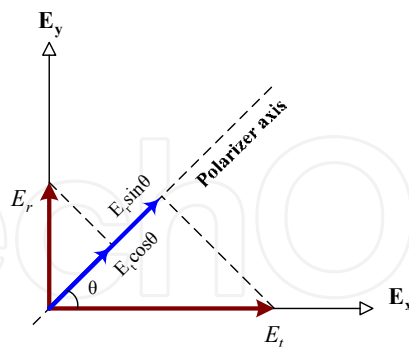

Fig. 5. Combination of orthogonally polarized beams on the linear polarizer
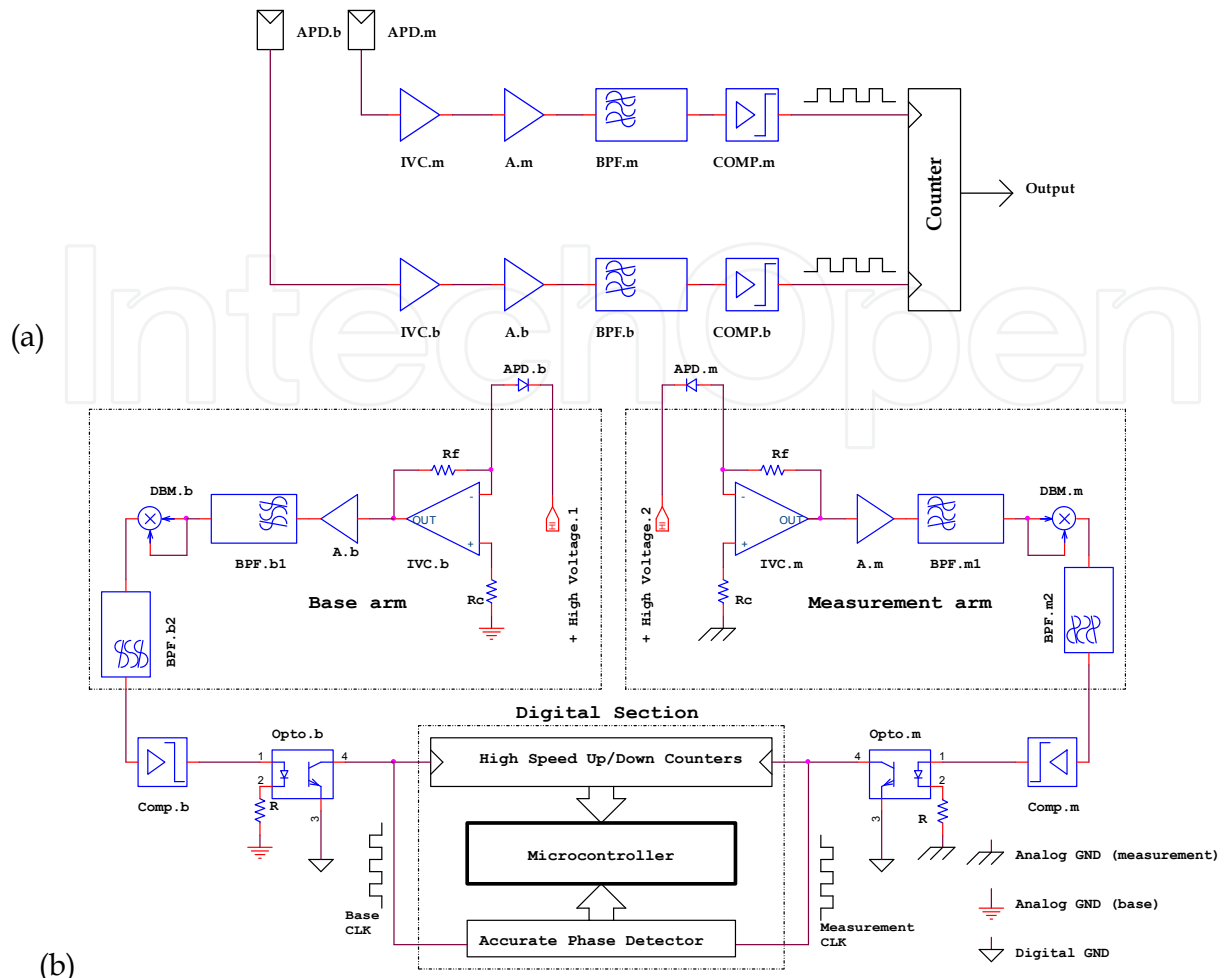
Fig. 6. The schematic of the electronic circuits of the nano-metrology system based on the (a) two- and (b) three-longitudinal-mode laser interferometers

Owing to the square-law behavior of the photodiodes, the reference signal is expressed as:

$$I_{APD_b} = A\cos(2\pi(\nu_3 - \nu_1)t) + B\cos(2\pi(\nu_3 - \nu_2)t) + C\cos(2\pi(\nu_2 - \nu_1)t) + D \qquad (26)$$
$$= A\cos(2\pi(f_{bH} + f_{bL})t) + B\cos(2\pi f_{bH}t) + C\cos(2\pi f_{bL}t) + D$$

Similarly, the output current of the measurement avalanche photodiode, APD_m, is:

$$I_{APD_m} = A\cos(2\pi(f_{bH} + f_{bL})t) + B\cos(2\pi(f_{bH} \mp \Delta f)t) + C\cos(2\pi(f_{bL} \pm \Delta f)t) + D \qquad (27)$$

where A, B, C, and D are constant values and Δf is the frequency shift due to the Doppler effect and its sign is dependent on the moving direction of the target. To extract the phase shift from Eqs. (26) and (27), two signals are fed to the proper electronic section as described in the following.

3.2 The Electronic Sections

The schematic diagram of the electronic circuits of the two- and three-longitudinal-mode laser interferometers are shown in Fig. 6. In both systems, the photocurrents of the avalanche photodiodes are amplified and converted to voltage signals. In two-mode system, the amplified signals pass through the band-pass filters (BPFs) involving the intermode beat frequency (typically several hundred MHz which can be reduced by heterodyne technique).

Parameter		Two-Longitudinal-Mode Laser Interferometer	Three-Longitudinal-Mode Laser Interferometer	Unit
Wavelength		632.8	632.8	nm
Cavity length		25	35	cm
Synthetic wavelength		0.5	1000	m
Maximum absolute distance		0.25	500	m
Intermode beat frequency		600	435.00, 435.30, 870.30	MHz
Secondary beat frequency		---	300	kHz
Maximum measurable velocity		21	0.047	m/s
Phase detection accuracy (similar circuit)		11.8	5.9	pm
Cross-talk and intermodulation distortion error		100	18	pm
The number of active frequency-path elements		4	6	
The number of distinct interference terms	Optical power	4	6	
	AC interference	2	6	
	DC interference	2 (Total: 10)	3 (Total: 21)	
	AC reference	2	6	

Table 2. A comparison between two- and three-longitudinal-mode He-Ne laser interferometers with typical values (Olyaee & Nejad, 2007c)

Two signals from base and measurement arms are then fed to a counter to measure the target displacement resulting from optical path difference.

But in TLMI, the amplified signals are self-multiplied by two double-balanced mixers, DBM_b and DBM_m. As a result, the secondary beat frequency generates (typically several hundred kHz). The high frequency and DC components are eliminated by two band-pass filters, BPF_{b2} and BPF_{m2}. The input signals of the comparators for base and measurement arms are respectively described as:

$$V_{ob} = k'\cos(2\pi f_s t) \tag{28}$$

$$V_{om} = k'\cos(2\pi f_s t - 2\Delta\Phi) \tag{29}$$

The phase shift resulting from optical path difference is measured by a high-speed up/down counter. The base and measurement signals can be exerted to a half exclusive-or gate and the pulse width is measured by a high speed counter. The phase difference between the base and measurement signals is proportional to the output pulse width. The

resolution of the phase detector is proportional to the clock pulse of the counter. The phase shift due to optical path difference is given by:

$$\Delta\Phi = \frac{4n\pi}{\lambda_2}\Delta z \tag{30}$$

where λ_2 is the central wavelength. It should be noted that in Eq. (29), the phase shift is multiplied by 2 which indicates the resolution in TLMI is doubled compared to two-mode type (see Eq. (17)).

On the other hand, the maximum measurable velocity corresponding to Eq. (18) is dependent on the intermode beat frequencies. In the TLMI, because we use super-heterodyne method to extract the secondary beat frequency (that is much smaller than primary beat frequencies produced in the TLMI or than intermode beat frequency in two-mode type), the maximum measurable velocity to be considerably reduced.

A comparison between two- and three-mode laser interferometers with typical values is summarized in Table 2. The maximum measurable velocity for two-mode type is about 21m/s, whereas in TLMI it is limited to 47.46mm/s. But according to Table 2, the resolution of the displacement measurement and synthetic wavelength in the three-longitudinal-mode is considerably increased. The output signals of the measurement double-balanced mixer and band-pass filter for fixed target, -47 mm/s, -20 mm/s, and +47 mm/s target velocities are shown in Fig. 7.

3.3 The Frequency-Path Modeling

A multi-path, multi-mode laser heterodyne interferometer can be described by a frequency-path (FP) model. The frequency-path models of two- and three-longitudinal-mode interferometers are shown in Fig. 8. In the measurement arm of TLMI, there are three frequency components and two paths namely the reference and the target (the bold lines are the main signal paths and the dashed lines are the leakage paths), whereas in two-longitudinal-mode interferometer, there are two frequency components and two paths. The number of active frequency-path elements, $\aleph$, is obtained by multiplying the number of frequency components by paths (Schmitz & Beckwith, 2003). Consequently, in two-path, two- and three-mode interferometers, the number of active FP elements is 4 and 6, respectively.

Figure 9 shows the identification of the physical origin of each frequency-path element for the measurement arms of two- and three-mode interferometers. Because the wave intensity being received by an APD is proportional to the square of the total electrical field, the number of distinct interference terms is equal to:

$$M = \frac{\aleph(\aleph+1)}{2} = 21 \tag{31}$$

In TLMI, the reference path field can be described by:

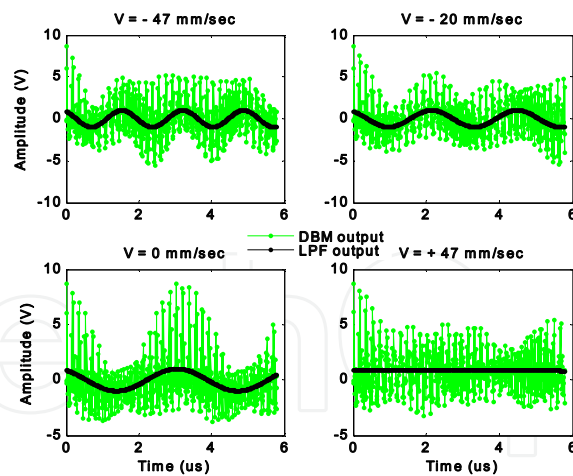$$E_i = E_{i1}\cos(\omega_i t - k_i z_1 + \varphi_{i1}) \quad , \quad i = 1,2,3 \tag{32}$$

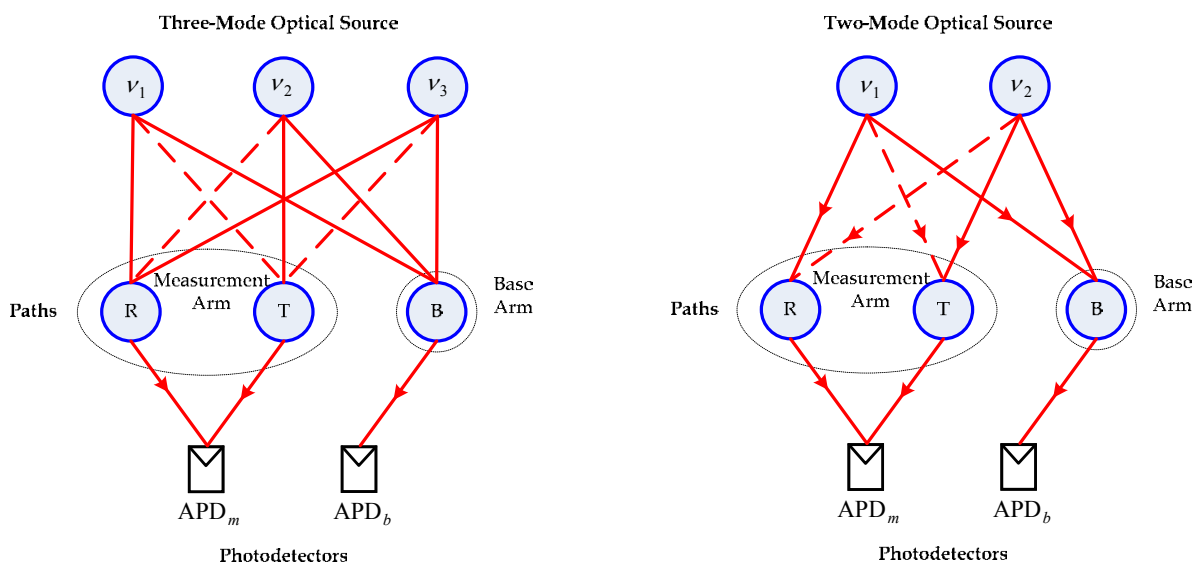Fig. 7. The output signals of the measurement BPF and DBM (Olyaee & Nejad, 2007b)

Fig. 8. The frequency-path model in two- and three-longitudinal-mode laser interferometers

where φ_{ij} is the initial phases corresponding to the electrical field E_{ij}, k_i is the propagation constant or wave number $\left(= 2\pi / \lambda_i\right)$, $\omega_i = 2\pi v_i$ is the optical angular frequency, and z_1 is the motion of the corner cube prism in the reference path (CCP_r). Similar to Eq. (32), the target path field is described by:

$$E_i = E_{i2} \cos(\omega_i t - k_i z_2 + \varphi_{i2}) \quad , \quad i = 1,2,3 \tag{33}$$

where z_2 is the motion of the corner cube prism in the target path (CCP_t). In this system, the CCP_r is fixed and hence, $z_1 = 0$. Furthermore, the wavelengths are so close that propagation constants become almost equal to each other ($k_1 = k_2 = k_3 = k$). The high frequency components such as ω_i, $2\omega_i$ and $\omega_i + \omega_j$ are eliminated by the avalanche photodiodes ($i, j = 1,2,3$). Therefore, ignoring the high frequencies in the fully unwanted leaking interferometers, there are 21 distinct interference terms for three-longitudinal-mode

interferometer and 10 distinct interference terms for two-mode type (see Table 2). The distinct interference terms can be divided into four groups namely dc interference (DI), ac interference (AI), ac reference (AR), and optical power (OP). These components in the three-longitudinal-mode interferometer are respectively given by (Olyaee & Nejad, 2007a):

$$I_{DI}/K = E_{11}\widetilde{E}_{12}\cos(kz_2) + \widetilde{E}_{21}E_{22}\cos(kz_2) + E_{31}\widetilde{E}_{32}\cos(kz_2)$$ (34)

$$I_{AI}/K = E_{11}E_{22}\cos(\omega_{bL}t - kz_2) + E_{11}\widetilde{E}_{32}\cos((\omega_{bH} + \omega_{bL})t - kz_2) + \widetilde{E}_{21}\widetilde{E}_{12}\cos(\omega_{bL}t + kz_2) +$$ (35)
$$\widetilde{E}_{21}\widetilde{E}_{32}\cos(\omega_{bH} - kz_2) + E_{31}\widetilde{E}_{12}\cos((\omega_{bH} + \omega_{bL})t + kz_2) + E_{31}E_{22}\cos(\omega_{bH}t + kz_2)$$

$$I_{AR}/K = \left(E_{11}\widetilde{E}_{21} + \widetilde{E}_{12}E_{22}\right)\cos(\omega_{bL}t) + \left(\widetilde{E}_{21}E_{31} + E_{22}\widetilde{E}_{32}\right)\cos(\omega_{bH}t)$$ (36)
$$+ \left(\widetilde{E}_{12}\widetilde{E}_{32} + E_{11}E_{31}\right)\cos((\omega_{bH} + \omega_{bL})t)$$

$$I_{OP}/K = \frac{1}{2}\left(E_{11}^2 + \widetilde{E}_{21}^2 + E_{31}^2 + \widetilde{E}_{12}^2 + E_{22}^2 + \widetilde{E}_{32}^2\right)$$ (37)

Figure 10 shows the combination of the frequency-path elements in the measurement arm of two systems. The main signals and leakages are depicted by large and small solid circles, respectively. On the other hand, the diameter of the circles presents the amplitude of the signals. The small solid circles are exaggerated for clarification. All of the distinct interference terms are shown in Fig. 10 by different lines.
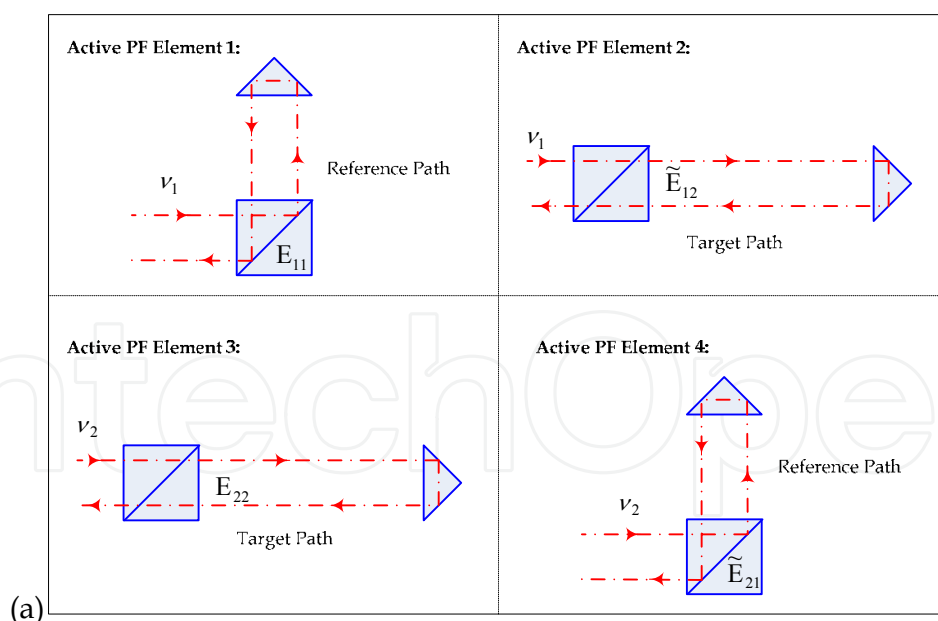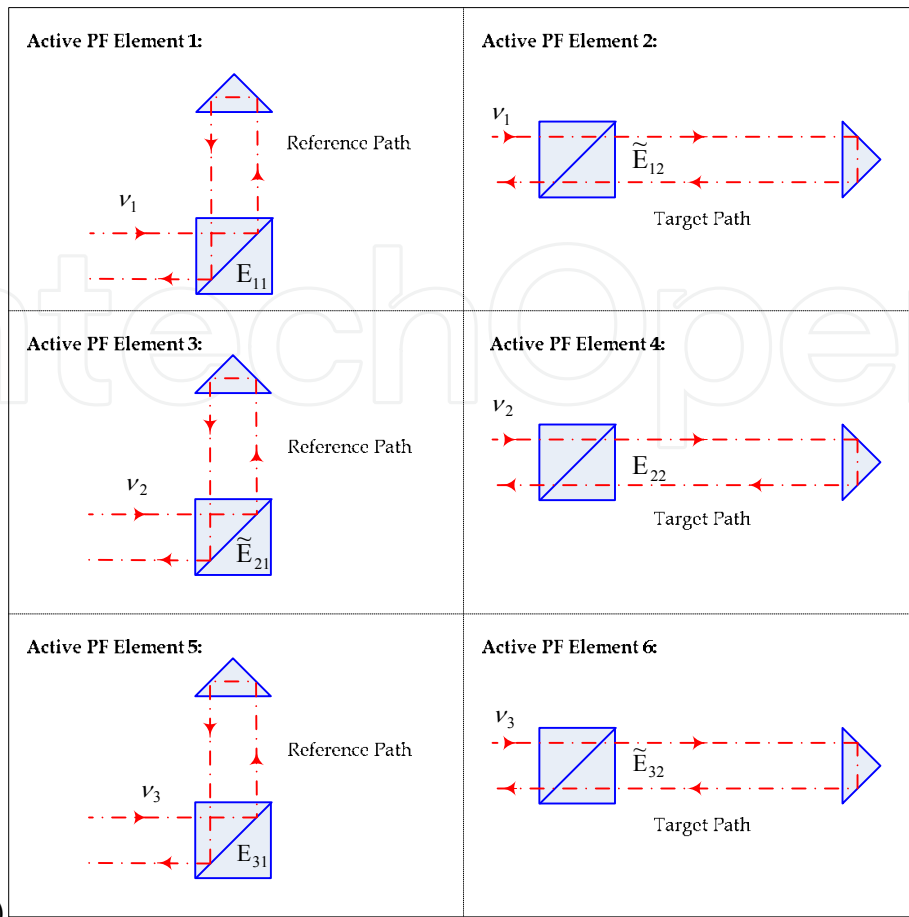
(b)

Fig. 9. Identification of the physical origin of each frequency-path element in the reference and target paths (measurement arms). (a) Two- and (b) Three-longitudinal-mode laser interferometers
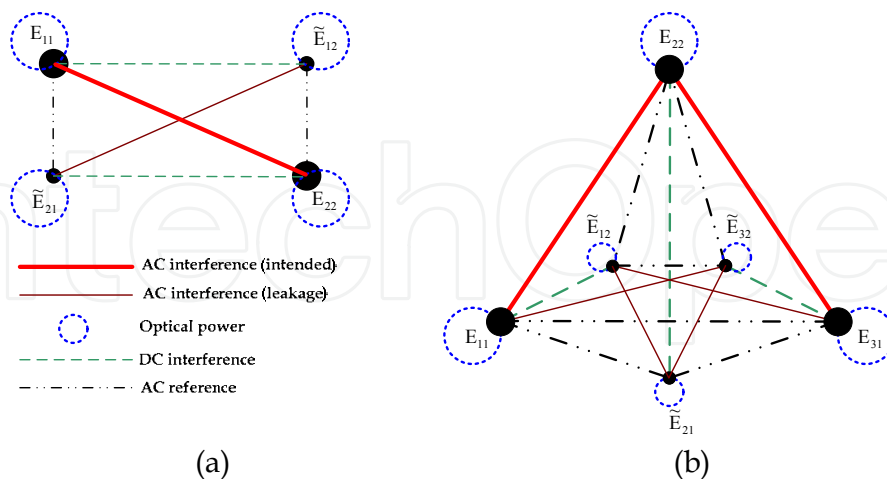
(a)   (b)

Fig. 10. The combination graph of the frequency-path elements in (a) two- and (b) three-longitudinal-mode interferometers

4. Nonlinearity Analysis

In section 2, we have shown that for a heterodyne interferometer the displacement could be determined by measuring the phase change between measurement and base signals. From Eq. (20), it can be seen that the accuracy of the displacement depends on the accuracy of the determination of the phase change, the wavelength of light and the refractive index of the medium. But, the displacement accuracy is also influenced far more by setup configuration, instrumentation section and environmental effects (Cosijns, 2004).

The first group is related to misalignment and deviations in the optical setup and components such as polarizer, polarizing-beam splitter and laser head. These can be minimized or even eliminated by using a correct setup and alignment procedures. In the second group related to electronic and instrumentation section includes laser frequency instability, phase detection error and data age uncertainty (Demarest, 1998). Instability in the mechanical instruments, cosine error and Abbe error are directly related to the setup configuration. The accuracy of refractive index determination, turbulences and thermal instability are the environmental parameters affecting the accuracy of the displacement (Bonsch & Potulski 1998; Wu, 2003; Edlen, 1966). In the mentioned errors, several of them are considered as linear errors that can be simply reduced or compensated.

When the measured displacement with a non-ideal interferometer is plotted against the real displacement of the moving target an oscillation around the ideal straight line is observed. This effect is known as a periodic deviation of the laser interferometer (Cosijns, 2004). The stability of the laser source, alignment error, vibration, temperature variation and air turbulence are the main sources of error for the optical interferometer. If all of the above conditions can be kept good enough, then the practical limitations will be given by the photonic noise and the periodic nonlinearity inherent in the interferometer (Wu & Su, 1996). The nonlinearity of one-frequency interferometry is a two-cycle phase error, whereas in heterodyne interferometry is mainly a one-cycle phase error as the optical path difference changes from 0 to 2π. Although the heterodyne interferometers have a larger nonlinearity than do the one-frequency interferometers, with first-order versus second-order error, the first-order nonlinearity of heterodyne interferometers can be compensated on-line (Wu et al, 1996).

In the ideal heterodyne interferometers, two beams are completely separated from each other and traverse with pure form in the two arms of the interferometer. Although the heterodyne method compared to the homodyne method provides more signal to noise ratio and easy alignment, in contrast, because of using two separated beams in the heterodyne method, the nonlinearity errors especially cross-talk and cross-polarization dominate. The polarization-mixing happens within an imperfect polarizing-beam splitter. This is nonlinearity error which is often in the one frequency interferometer. Meanwhile in case of heterodyne laser interferometer, frequency mixing error which arises from non-orthogonality of the polarizing radiations, elliptical polarization and imperfect alignment of the laser head and other components produce periodic nonlinearity error (Cosijns et al., 2002; Freitas, 1997; Eom et al. 2001; Hou & Wilkening 1992; Meyers et al., 2001; Sutton, 1998). The two waves, which are regarded as orthogonal to each other in a heterodyne interferometer, are not perfectly separated by the polarizing-beam splitter, with the result that the two frequencies are mixed. The mixing leads to a nonlinear relationship between the measured phase and the actual phase, and limits the accuracy of the heterodyne interferometer with a two-frequency laser to a few nanometers. The periodic nonlinearity can be analytically modeled by both Jones calculus and plane wave which will be described in the next two sections.

4.1 Analytical Modeling of the Periodic Nonlinearity based Jones Calculus

According to the setup of TLMI in Fig. 4b, in both paths of the reference (reflected) and target paths (transmitted), there are small fractions of oppositely polarized beams as a leakage caused by the ellipticity of the laser mode polarization and misalignment of the polarization axes between the laser beam and PBS. The leakage beams result in the frequency mixing and produce the periodic nonlinearity in the detected heterodyne signal. To have a model of nonlinearity in the TLMI, we first assume that the beam emerged from the laser is to be elliptically polarized. The ellipticity of the central and side modes are denoted by δ_{ε_t} and δ_{ε_r}, respectively, as usual. Then, the electric fields of three longitudinal modes are respectively given as:

$$\vec{\mathbf{E}}_1 = \begin{pmatrix} \cos\delta_{\varepsilon_r} \\ i\sin\delta_{\varepsilon_r} \end{pmatrix} \exp i\left(\omega_1 t + \varphi_{0_1}\right) \tag{38}$$

$$\vec{\mathbf{E}}_2 = -\begin{pmatrix} i\sin\delta_{\varepsilon_t} \\ \cos\delta_{\varepsilon_t} \end{pmatrix} \exp i\left(\omega_2 t + \varphi_{0_2}\right) \tag{39}$$

$$\vec{\mathbf{E}}_3 = \begin{pmatrix} \cos\delta_{\varepsilon_r} \\ i\sin\delta_{\varepsilon_r} \end{pmatrix} \exp i\left(\omega_3 t + \varphi_{0_3}\right) \tag{40}$$

If the rotation angle of the PBS with respect to the laser polarization axis is denoted by α, the matrix representing the PBS for reference and target beam directions respectively can be calculated as :

$$\mathbf{RPBS} = \begin{pmatrix} \cos\alpha & -\sin\alpha \\ \sin\alpha & \cos\alpha \end{pmatrix} \begin{pmatrix} 1 & 0 \\ 0 & 0 \end{pmatrix} \begin{pmatrix} \cos\alpha & \sin\alpha \\ -\sin\alpha & \cos\alpha \end{pmatrix} \tag{41}$$

$$\mathbf{TPBS} = \begin{pmatrix} \cos\alpha & -\sin\alpha \\ \sin\alpha & \cos\alpha \end{pmatrix} \begin{pmatrix} 0 & 0 \\ 0 & 1 \end{pmatrix} \begin{pmatrix} \cos\alpha & \sin\alpha \\ -\sin\alpha & \cos\alpha \end{pmatrix} \tag{42}$$
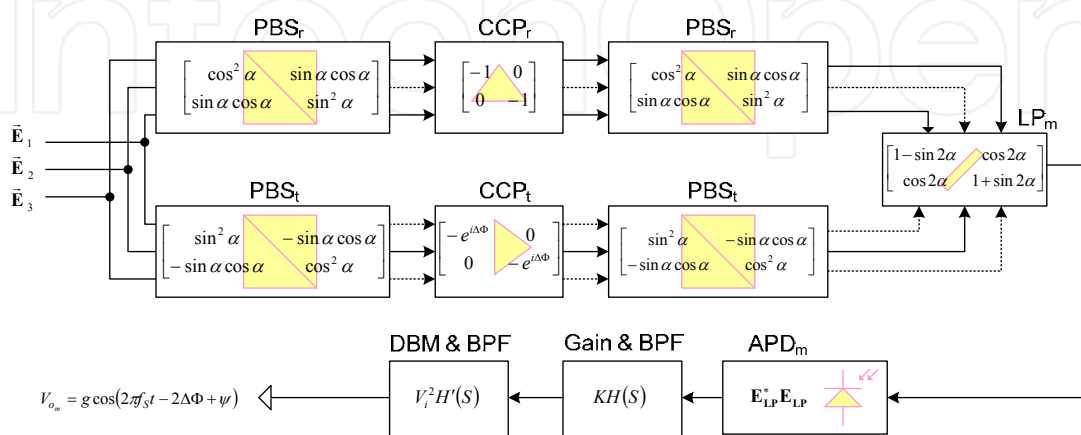

Fig. 11. Jones matrix components of the measurement arm of the TLMI with leakage fields. The dashed lines indicate optical leakage

The Jones matrix for linear polarizer oriented at 45° relative to the polarization directions is then described by:

$$\mathbf{LP} = \begin{pmatrix} \cos^2(45+\alpha) & \cos(45+\alpha)\sin(45+\alpha) \\ \cos(45+\alpha)\sin(45+\alpha) & \sin^2(45+\alpha) \end{pmatrix} \tag{43}$$

Figure 11 shows the simplified matrices for optical components of the target and reference paths including the optical leakages in the TLMI. The optical leakages are shown by dashed lines (Olyaee et al., 2009).

According to Fig. 11, the Jones vector of the reference electrical field incident upon the linear polarizer is obtained as:

$$\vec{\mathbf{E}}_{\mathbf{r}} = \mathbf{RPBS.RCCP.RPBS} \sum_{l=1}^{3} \vec{\mathbf{E}}_l \tag{44}$$

where $\mathbf{RCCP}$ is the Jones matrix for reference corner cube prism (CCP$_r$) in the reference path which is given by:

$$\mathbf{RCCP} = \begin{pmatrix} -1 & 0 \\ 0 & -1 \end{pmatrix} \tag{45}$$

If the reflection coefficient of the PBS in the reference path direction is denoted as ρ, by substitution of the related Jones matrices, Eq. (44) can be rewritten as:

$$\vec{\mathbf{E}}_{\mathbf{r}} = \rho \begin{pmatrix} -\cos^2\alpha\cos\delta_{\varepsilon_r} - i\sin\alpha\cos\alpha\sin\delta_{\varepsilon_r} & i\cos^2\alpha\sin\delta_{\varepsilon_t} + \sin\alpha\cos\alpha\cos\delta_{\varepsilon_t} \\ -\sin\alpha\cos\alpha\cos\delta_{\varepsilon_r} - i\sin^2\alpha\sin\delta_{\varepsilon_r} & i\sin\alpha\cos\alpha\sin\delta_{\varepsilon_t} + \sin^2\alpha\cos\delta_{\varepsilon_t} \end{pmatrix} \times$$
$$\begin{pmatrix} \exp i(\omega_1 t + \varphi_{0_1}) + \exp i(\omega_3 t + \varphi_{0_3}) \\ \exp i(\omega_2 t + \varphi_{0_2}) \end{pmatrix} \tag{46}$$

Similar to Eq. (44), the target electrical field is given by:

$$\vec{\mathbf{E}}_{\mathbf{t}} = \mathbf{TPBS.TCCP.TPBS} \sum_{l=1}^{3} \vec{\mathbf{E}}_l$$
$$= \tau \begin{pmatrix} -\sin^2\alpha\cos\delta_{\varepsilon_r} + i\sin\alpha\cos\alpha\sin\delta_{\varepsilon_r} & i\sin^2\alpha\sin\delta_{\varepsilon_t} - \sin\alpha\cos\alpha\cos\delta_{\varepsilon_t} \\ \sin\alpha\cos\alpha\cos\delta_{\varepsilon_r} - i\cos^2\alpha\sin\delta_{\varepsilon_r} & -i\sin\alpha\cos\alpha\sin\delta_{\varepsilon_t} + \cos^2\alpha\cos\delta_{\varepsilon_t} \end{pmatrix} \times$$
$$\begin{pmatrix} \exp i(\omega_1 t + \varphi_{0_1} + \Delta\Phi) + \exp i(\omega_3 t + \varphi_{0_3} + \Delta\Phi) \\ \exp i(\omega_2 t + \varphi_{0_2} + \Delta\Phi) \end{pmatrix} \tag{47}$$

where τ is the transmission coefficient of the PBS in the target path direction and $\mathbf{TCCP}$ is the Jones matrix for corner cube prism in the target path which is given by:

$$\mathbf{TCCP} = \begin{pmatrix} -\exp(i\Delta\Phi) & 0 \\ 0 & -\exp(i\Delta\Phi) \end{pmatrix} \tag{48}$$

The reflected beam of the reference path and the transmitted beam from the target path at the output port of the PBS interfere with each other through the linear polarizer. Therefore, the final electric field vector after passing through the linear polarizer (LP) is obtained by:

$$\vec{E}_{LP} = LP\left(\vec{E}_t + \vec{E}_r\right) \tag{49}$$

The intensity of the laser beam which is proportional of the photocurrent at the detector can be obtained by pre-multiplying the Jones vector with its complex conjugate of the matrix transpose. Consequently, the photocurrent detected by an avalanche photodiode can be given as:

$$I_{APD_m} \propto \vec{E}^*_{LP_X}\vec{E}_{LP_X} + \vec{E}^*_{LP_Y}\vec{E}_{LP_Y} \tag{50}$$

where $\vec{E}_{LP_X}$ and $\vec{E}_{LP_Y}$ are the X and Y components of the total electric field vector, respectively. By expanding Eq. (50) and eliminating the optical frequencies and dc component, the Fourier spectrum components and phase terms of the time-dependent photocurrent is obtained as:

$$\begin{aligned}
I_{APD_m} = &(e+ia)\left(e^{-i\omega_{bL}t} + e^{i\omega_{bH}t}\right) + (e-ia)\left(e^{i\omega_{bL}t} + e^{-i\omega_{bH}t}\right) + \\
&+ (b+ic)\left(e^{-i(\omega_{bL}t+\Delta\Phi)} + e^{i(\omega_{bH}t-\Delta\Phi)}\right) + (d-ic)\left(e^{i(\omega_{bL}t-\Delta\Phi)} + e^{-i(\omega_{bH}t+\Delta\Phi)}\right) + \\
&+ (d+ic)\left(e^{-i(\omega_{bL}t-\Delta\Phi)} + e^{i(\omega_{bH}t+\Delta\Phi)}\right) + (b-ic)\left(e^{i(\omega_{bL}t+\Delta\Phi)} + e^{-i(\omega_{bH}t-\Delta\Phi)}\right)
\end{aligned} \tag{51}$$

where

$$\begin{aligned}
e+ia &= A_X B^*_X + C_X D^*_X + A_Y B^*_Y + C_Y D^*_Y \\
e-ia &= B_X A^*_X + D_X C^*_X + B_Y A^*_Y + D_Y C^*_Y \\
b+ic &= A_X D^*_X + A_Y D^*_Y \\
d-ic &= B_X C^*_X + B_Y C^*_Y \\
d+ic &= C_X B^*_X + C_Y B^*_Y \\
b-ic &= D_X A^*_X + D_Y A^*_Y
\end{aligned} \tag{52}$$

and

$$\begin{aligned}
A_X / \rho = &(\sin 2\alpha - 1)\left(\cos^2\alpha\cos\delta_{\varepsilon_r} + i\sin\alpha\cos\alpha\sin\delta_{\varepsilon_r}\right) \\
&- \cos 2\alpha\left(\sin\alpha\cos\alpha\cos\delta_{\varepsilon_r} + i\sin^2\alpha\sin\delta_{\varepsilon_r}\right)
\end{aligned} \tag{53}$$

$$\begin{aligned}
B_X / \rho = &(1 - \sin 2\alpha)\left(i\cos^2\alpha\sin\delta_{\varepsilon_t} + \sin\alpha\cos\alpha\cos\delta_{\varepsilon_t}\right) \\
&+ \cos 2\alpha\left(i\sin\alpha\cos\alpha\sin\delta_{\varepsilon_t} + \sin^2\alpha\cos\delta_{\varepsilon_t}\right)
\end{aligned} \tag{54}$$

$$\begin{aligned}
C_X / \tau = &(1 - \sin 2\alpha)\left(-\sin^2\alpha\cos\delta_{\varepsilon_r} + i\sin\alpha\cos\alpha\sin\delta_{\varepsilon_r}\right) \\
&+ \cos 2\alpha\left(\sin\alpha\cos\alpha\cos\delta_{\varepsilon_r} - i\cos^2\alpha\sin\delta_{\varepsilon_r}\right)
\end{aligned} \tag{55}$$

$$\begin{aligned}
D_X / \tau = &(1 - \sin 2\alpha)\left(i\sin^2\alpha\sin\delta_{\varepsilon_t} - \sin\alpha\cos\alpha\cos\delta_{\varepsilon_t}\right) \\
&+ \cos 2\alpha\left(-i\sin\alpha\cos\alpha\sin\delta_{\varepsilon_t} + \cos^2\alpha\cos\delta_{\varepsilon_t}\right)
\end{aligned} \tag{56}$$

$$\begin{aligned}
A_Y / \rho = &-\cos 2\alpha\left(\cos^2\alpha\cos\delta_{\varepsilon_r} + i\sin\alpha\cos\alpha\sin\delta_{\varepsilon_r}\right) \\
&- (1 + \sin 2\alpha)\left(\sin\alpha\cos\alpha\cos\delta_{\varepsilon_r} + i\sin^2\alpha\sin\delta_{\varepsilon_r}\right)
\end{aligned} \tag{57}$$

$$B_Y / \rho = \cos 2\alpha \left(i \cos^2 \alpha \sin \delta_{\varepsilon_t} + \sin \alpha \cos \alpha \cos \delta_{\varepsilon_t} \right)$$
$$+ \left(1 + \sin 2\alpha \right) \left(i \sin \alpha \cos \alpha \sin \delta_{\varepsilon_t} + \sin^2 \alpha \cos \delta_{\varepsilon_t} \right) \tag{58}$$

$$C_Y / \tau = \cos 2\alpha \left(-\sin^2 \alpha \cos \delta_{\varepsilon_r} + i \sin \alpha \cos \alpha \sin \delta_{\varepsilon_r} \right)$$
$$+ \left(1 + \sin 2\alpha \right) \left(\sin \alpha \cos \alpha \cos \delta_{\varepsilon_r} - i \cos^2 \alpha \sin \delta_{\varepsilon_r} \right) \tag{59}$$

$$D_Y / \tau = \cos 2\alpha \left(i \sin^2 \alpha \sin \delta_{\varepsilon_t} - \sin \alpha \cos \alpha \cos \delta_{\varepsilon_t} \right)$$
$$+ \left(1 + \sin 2\alpha \right) \left(-i \sin \alpha \cos \alpha \sin \delta_{\varepsilon_t} + \cos^2 \alpha \cos \delta_{\varepsilon_t} \right) \tag{60}$$

Finally, Eq. (51) can be simplified as:

$$I_{APD_m} = a \left(\sin(\omega_{bL} t) - \sin(\omega_{bH} t) \right) + b \left(\cos(\omega_{bH} t - \Delta\Phi) + \cos(\omega_{bL} t + \Delta\Phi) \right)$$
$$+ c \left(\sin(\omega_{bL} t + \Delta\Phi) - \sin(\omega_{bH} t - \Delta\Phi) + \sin(\omega_{bL} t - \Delta\Phi) - \sin(\omega_{bH} t + \Delta\Phi) \right)$$
$$+ d \left(\cos(\omega_{bL} t - \Delta\Phi) + \cos(\omega_{bH} t + \Delta\Phi) \right) + e \left(\cos(\omega_{bL} t) + \cos(\omega_{bH} t) \right) \tag{61}$$

As shown in Fig. 6b, the photocurrent of the APD is further processed for the super-heterodyning by using a double-balanced mixer (DBM) and band-pass filter (BPF). Because of using the BPF, the higher frequency component and the dc component of the photocurrent can be effectively filtered out, resulting in the detection of a heterodyne signal oscillating only at the secondary beat frequency with a high signal-to-noise ratio. Thus, the output voltage is proportional to:

$$V'_{o_m} = \left(-a^2 + 2bd - 2c^2 + e^2 \right) \cos(\omega_S t) - 2(ab + ce) \sin(\omega_S t - \Delta\Phi)$$
$$- 2(ac - be) \cos(\omega_S t - \Delta\Phi) - 2(cb + cd + ae) \sin(\omega_S t) - 2(ad + ce) \sin(\omega_S t + \Delta\Phi)$$
$$- 2(ac - de) \cos(\omega_S t + \Delta\Phi) - 2bc \sin(\omega_S t - 2\Delta\Phi) - 2cd \sin(\omega_S t + 2\Delta\Phi)$$
$$+ \left(b^2 - c^2 \right) \cos(\omega_S t - 2\Delta\Phi) + \left(d^2 - c^2 \right) \cos(\omega_S t + 2\Delta\Phi) \tag{62}$$

To extract the phase nonlinearity from the above analytical formula, Eq. (62) could be simplified as:

$$V_m = D \cos(\omega_S t - 2\Delta\Phi) + N \sin(\omega_S t + 2\Delta\Phi) = \sqrt{D^2 + N^2} \cos\left(\omega_S t - 2\Delta\Phi - \tan^{-1} \frac{N}{D} \right) \tag{63}$$

where

$$D = \left(-a^2 + 2bd - 2c^2 + e^2 \right) \cos 2\Delta\Phi - 2(ab + ce) \sin \Delta\Phi$$
$$- 2(ac - be) \cos \Delta\Phi - 2(cb + cd + ae) \sin 2\Delta\Phi - 2(ad + ce) \sin 3\Delta\Phi$$
$$- 2(ac - de) \cos 3\Delta\Phi - 2cd \sin 4\Delta\Phi + \left(b^2 - c^2 \right) + \left(d^2 - c^2 \right) \cos 4\Delta\Phi, \tag{64}$$

$$N = \left(a^2 - 2bd + 2c^2 - e^2 \right) \sin 2\Delta\Phi - 2(ab + ce) \cos \Delta\Phi$$
$$+ 2(ac - be) \sin \Delta\Phi - 2(cb + cd + ae) \cos 2\Delta\Phi - 2(ad + ce) \cos 3\Delta\Phi$$
$$+ 2(ac - de) \sin 3\Delta\Phi - 2bc - 2cd \cos 4\Delta\Phi - \left(d^2 - c^2 \right) \sin 4\Delta\Phi, \tag{65}$$

And the phase nonlinearity can be finally calculated as:

$$\psi = -\tan^{-1} \frac{N}{D} \tag{66}$$

This nonlinearity causes to appear the periodic nonlinearity in the displacement measurement.

4.2 Analytical Modeling of the Periodic Nonlinearity based Plane Waves

Another method for nonlinearity modeling is based on the plane wave method. By using these approaches, a similar model for periodic nonlinearity is obtained. Here, the electrical field vectors of side modes, $\vec{E}_{1,3}$, and central mode, $\vec{E}_2$, emerging from the three-longitudinal-mode laser source with ellipticity of the reference and target beams are respectively given as:

$$\vec{E}_{1,3} = \cos\delta_{\varepsilon_r} E_{01}\left(\sin(2\pi v_1 t + \varphi_{01}) + \sin(2\pi v_3 t + \varphi_{03})\right) - \sin\delta_{\varepsilon_r} E_{02}\cos(2\pi v_2 t + \varphi_{02}) \tag{67}$$

$$\vec{E}_2 = \sin\delta_{\varepsilon_i} E_{01}(\cos(2\pi v_1 t + \varphi_{01}) + \cos(2\pi v_3 t + \varphi_{03})) - \cos\delta_{\varepsilon_i} E_{02}\sin(2\pi v_2 t + \varphi_{02}) \tag{68}$$

Considering the non-orthogonality of the polarized beams in combination with the deviation angle of PBS with respect to the laser head, α and β, a leakage of modes appears. The electrical field magnitudes of the transmitted and reflected beams by the PBS are given by:

$$\vec{E}_t = \tau\begin{pmatrix} \sin\beta \\ \cos\alpha \end{pmatrix} \times \left[E_{13}(x_i + \phi_t)E_2(x_i + \phi_t)\right] \tag{69}$$

$$\vec{E}_r = \rho\begin{pmatrix} \sin\beta \\ \cos\alpha \end{pmatrix} \times \left[E_{13}(x_i + \phi_r)E_2(x_i + \phi_r)\right] \tag{70}$$

Here the terms $2\pi v_i t + \varphi_{0i}$ denoted by x_i, $i = 1,2,3$ and τ and ρ are the transmission and reflection coefficients of the PBS and φ_t and φ_r are the optical phase shift in the target and reference paths, respectively. If the deviation angle of polarizer referred to $45°$ is represented as θ, the output of measurement photocurrent is corrected as:

$$I_{APD_m} \propto \left|E_r\cos(45-\theta) + E_t\sin(45-\theta)\right|^2 \tag{71}$$

With detection of secondary beat frequency by the super-heterodyne detection, the nonlinearity phase error is concluded similar to Eq. 66:

$$\begin{aligned} V_m = C_1\sin x_s + C_2\cos x_s + C_3\sin(x_s - \Delta\Phi) + C_4\cos(x_s - \Delta\Phi) + C_5\sin(x_s + \Delta\Phi) + \\ C_6\cos(x_s + \Delta\Phi) + C_7\sin(x_s - 2\Delta\Phi) + C_8\cos(x_s - 2\Delta\Phi) + C_9\sin(x_s + 2\Delta\Phi) + C_{10}\cos(x_s + 2\Delta\Phi) \end{aligned} \tag{72}$$

where

$$\begin{aligned} C_1 &= 2\left(A_1 A_2 + B_1 B_3 + B_1 B_2\right) \\ C_2 &= A_1^2 - A_2^2 + 2B_1^2 - 2B_2 B_3 \\ C_3 &= 2\left(A_1 B_2 + A_2 B_1\right) \\ C_4 &= 2\left(A_1 B_1 - A_2 B_2\right) \\ C_5 &= 2\left(A_1 B_3 + A_2 B_1\right) \\ C_6 &= 2\left(A_1 B_1 - A_2 B_3\right) \end{aligned} \tag{73}$$

$$C_7 = 2B_1B_2$$
$$C_8 = B_1^2 - B_2^2$$
$$C_9 = 2B_1B_3$$
$$C_{10} = B_1^2 - B_3^2$$

and

$$A_1 = \sin\delta_{\varepsilon_r}\cos\delta_{\varepsilon_t}(K_2\cos^2\alpha + K_1\sin^2\alpha) - \cos\delta_{\varepsilon_r}\sin\delta_{\varepsilon_t}(K_2\sin^2\beta + K_1\cos^2\beta)$$
$$A_2 = (K_1\sin\alpha\cos\beta + K_2\cos\alpha\sin\beta)\cos(\delta_{\varepsilon_t} - \delta_{\varepsilon_r})$$
$$B_1 = K_3(-\cos\beta\sin\beta\cos\delta_{\varepsilon_r}\sin\delta_{\varepsilon_t} + \sin\alpha\cos\alpha\sin\delta_{\varepsilon_r}\cos\delta_{\varepsilon_t})$$
$$B_2 = K_3(\sin\alpha\sin\beta\sin\delta_{\varepsilon_r}\sin\delta_{\varepsilon_t} + \cos\alpha\cos\beta\cos\delta_{\varepsilon_r}\cos\delta_{\varepsilon_t})$$
$$B_3 = K_3(\cos\alpha\cos\beta\sin\delta_{\varepsilon_r}\sin\delta_{\varepsilon_t} + \sin\alpha\sin\beta\cos\delta_{\varepsilon_r}\cos\delta_{\varepsilon_t})$$
$$K_1 = \rho^2 E_{0_{1,3}}E_{0_2}\cos^2(45-\theta)$$
$$K_2 = \tau^2 E_{0_{1,3}}E_{0_2}\sin^2(45-\theta)$$
$$K_3 = \tau\rho E_{0_{1,3}}E_{0_2}\sin(45-\theta)\cos(45-\theta)$$
(74)

Here the nonlinearity is given by Eq. (66) and following equations:

$$N = C_1\cos(2\Delta\Phi) - C_2\sin(2\Delta\Phi) + C_3\cos(\Delta\Phi)$$
$$- C_4\sin(\Delta\Phi) + C_5\cos(3\Delta\Phi) - C_6\sin(3\Delta\Phi) + C_7 + C_9\cos(4\Delta\Phi) - C_{10}\sin(4\Delta\Phi)$$
(75)

$$D = C_1\sin(2\Delta\Phi) + C_2\cos(2\Delta\Phi) + C_3\sin(\Delta\Phi) + C_4\cos(\Delta\Phi)$$
$$+ C_5\sin(3\Delta\Phi) + C_6\cos(3\Delta\Phi) + C_8 + C_9\sin(4\Delta\Phi) + C_{10}\cos(4\Delta\Phi)$$
(76)

4.3 Error Analysis in the TLMI
Deviation angle and unequal transmission- reflection coefficients of the PBS
Considering the orthogonal linearly polarized modes, the effect of the PBS deviation angle is described by $\alpha = -\beta$. The periodic nonlinearities in terms of the nanometric displacement in the TLMI and two-mode interferometer are respectively illustrated in Fig. 12a and 12b. The range of displacement is equal to the one wavelength of the He–Ne laser at 632.8 nm. The result appears as the second-order nonlinearity. If the transmission and reflection coefficients of the PBS are equal, then the periodic nonlinearity does not change. The unequal coefficients and the mismatch between the factors causes the first-order nonlinearity dominates, as shown in Fig. 12c (curve 3).

Non-orthogonality associated with deviation angle of the PBS
If there is non-orthogonality even in the absence of deviation angle, there will be a leakage of modes. The effect of non-orthogonality of the polarized modes in combination with the deviation angle of PBS is represented by $\alpha \neq -\beta$ and is shown in Fig. 12d. Unlike Fig. 12a, the periodic nonlinearity due to the non-orthogonality of polarized modes is represented as the first order nonlinearity (see curve 1 in Fig. 12d for orthogonality).

Non-orthogonality in combination with ellipticity of adjacent polarized modes

Considering the TLMI free of nonlinearity except for one-ellipticity of the polarizations $\delta_{\varepsilon_t} = 0$, and two-elliptical polarized modes, the periodic nonlinearity is the first-order type of nonlinearity. But, if ellipticity of the polarized modes occurs simultaneously with orthogonality, it may reproduce the second-order nonlinearity (see curves 2 and 3 in Fig. 12e). The nonlinearity generated in the displacement measurement in one fourth of the laser wavelength range (158.2 nm) resulting from the ellipticity of laser polarization states for ideal alignment ($\alpha = 0$ deg) and non-ideal alignment ($\alpha = 3$ deg) are compared in Fig. 13. The nonlinearity error increases with increasing misalignment.

Rotation angle of the polarizer

A small rotation angle of the polarizer can provide nonlinearity, it can be appropriately utilized for nonlinearity compensation in a proper optical setup. The nonlinearity resulting from the two-ellipticity of the adjacent orthogonal and non-orthogonal polarized modes associated with the rotation angle of the polarizer is shown in Fig. 12f.
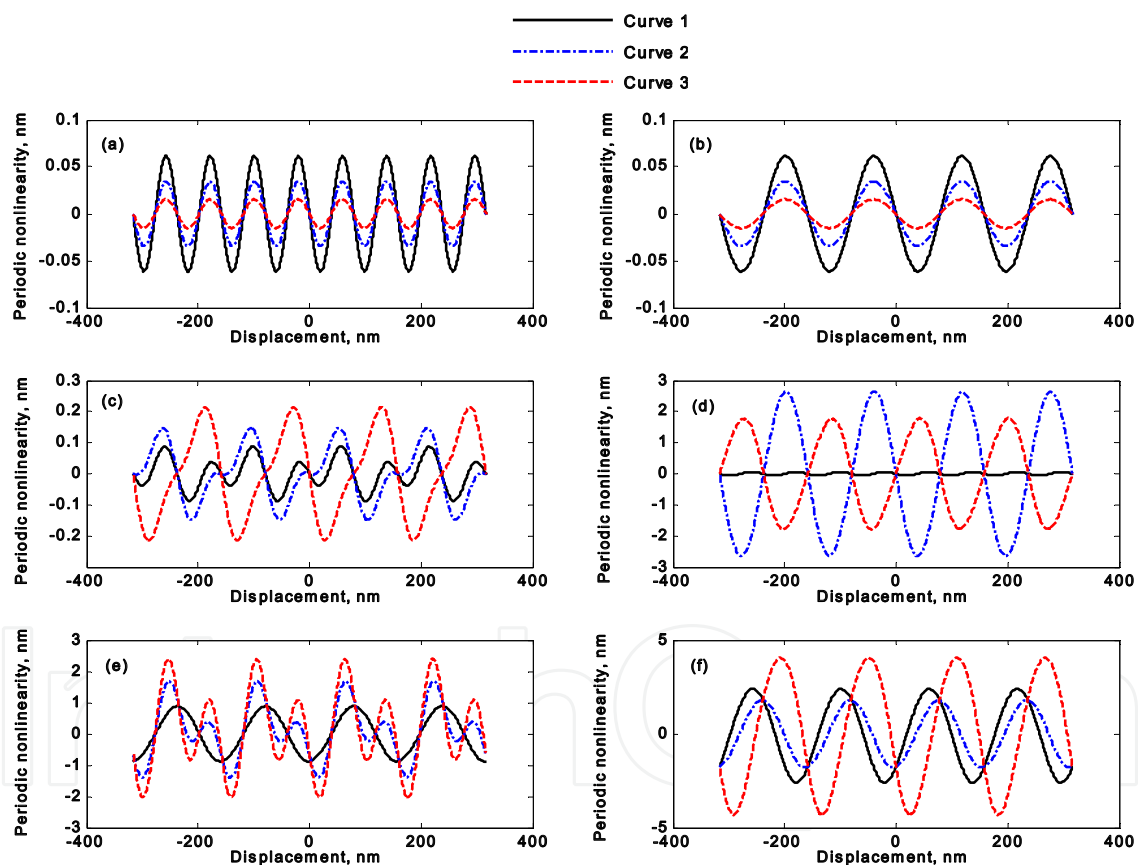
Fig. 12. Periodic nonlinearity resulting from various optical deviations. The orthogonal linearly polarized modes in the (a) three-mode interferometer and (b) two-mode interferometer. (c) Orthogonal linearly polarized modes in combination with unequal transmission and reflection coefficients. (d) The orthogonal (curve 1) and non-orthogonal (curves 2 and 3) linearly polarized modes in combination with deviation angle of PBS. (e) One-ellipticity of the adjacent orthogonal polarized modes. (f) Two-ellipticity of the adjacent orthogonal (curve 2) and non-orthogonal (curves 1 and 3) polarized modes in combination with the rotation angle of polarizer
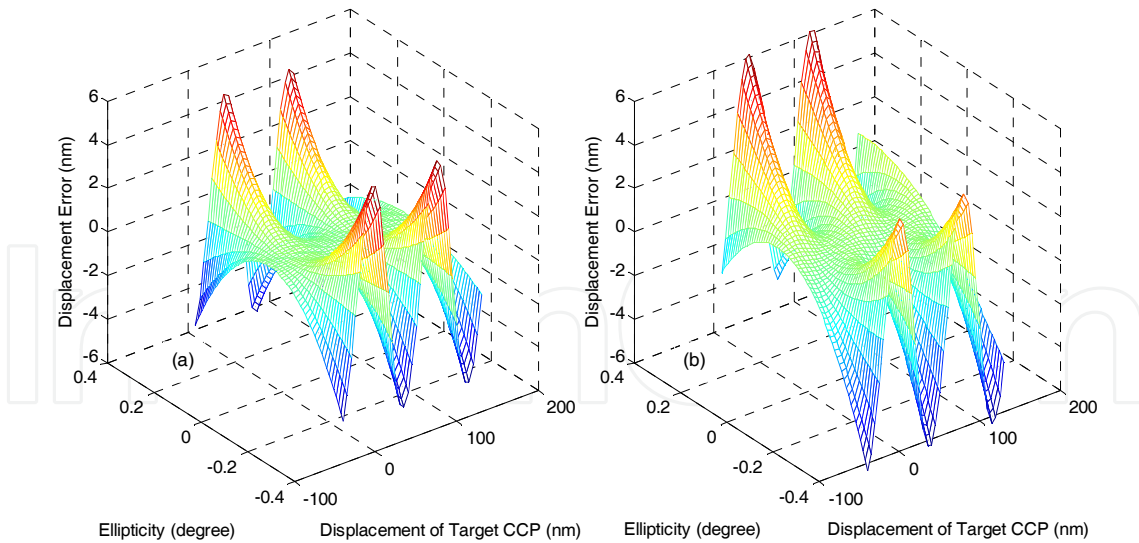
Fig. 13. The error of displacement measurement resulting from ellipticity of laser polarization states for (a) ideal alignment ($\alpha = 0^\circ$) and (b) non-ideal alignment ($\alpha = 3^\circ$)
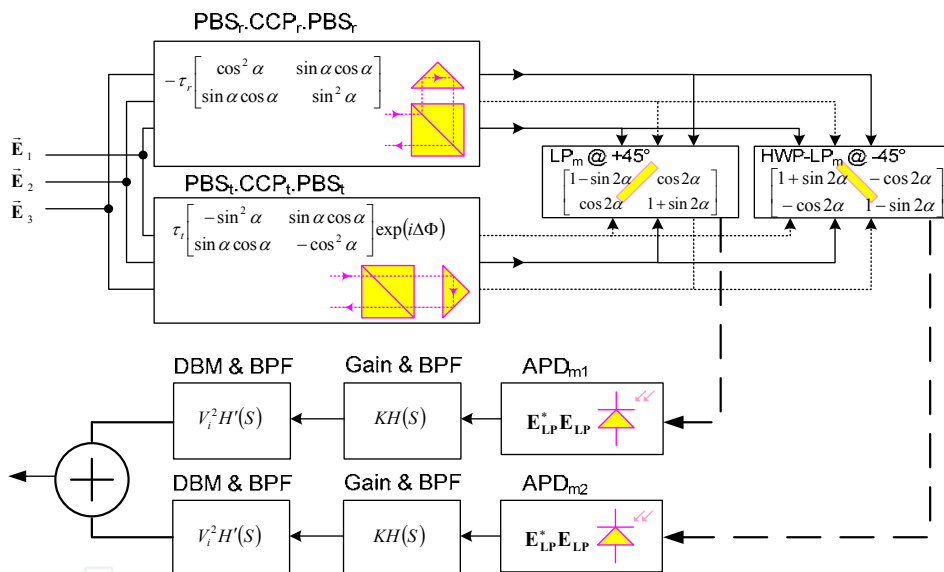

Fig. 14. The block diagram of nonlinearity reduction system

4.4 Nonlinearity Reduction

To reduce the nonlinearity in two-mode heterodyne interferometers, various kinds of heterodyning systems and methods are still being developed (Wuy & Su, 1996; Freitas, 1997; Wu, 2003; Badami & Patterson, 2000; Lin et al., 2000; Hou, 2006; Hou, & Zhaox, 1994). A basic block diagram of the optical and electrical nonlinearity reduction system designed for TLMI is schematically represented in Fig. 14. Two linear polarizers oriented at $+45^\circ$ and -45°, two avalanche photodiodes and a half-wave plate is used in the measurement arm. The current-to-voltage converter, pre-amplifier and band-pass filter is denoted by transfer function KH(S).

The output voltage is led to the double-balanced mixer and other band-pass filter to extract the secondary beat frequency. The electrical cross-talk error occurs due to the unwanted

induction between the electrical section of the base and measurement arms. This error can be reduced by: (i) coupling reduction between the base and measurement arms using a proper shielding, grounding and utilizing two isolated power supplies, (ii) noise reduction by using electromagnetic interference shield, (iii) electrical power reduction and (iv) utilizing the band pass filters with high quality factors.

A schematic diagram of the nano-displacement measurement based on the TLMI with noise and electrical error reduction is shown in Fig. 15. The unwanted electrical induction between the base and measurement paths is reduced by using two isolated power supplies for APD biasing and by separating the grounds (analogue-base, analogue-measurement and digital grounds). Due to switching noise of digital section including frequency and phase measurement circuits and microcontroller, two high-speed opto-couplers isolate the analogue circuits from digital section.

In order to reduce the periodic nonlinearity, two output signals can be averaged as shown in Fig. 14. Therefore noise and electrical cross-talk are considerably reduced.

The corresponding compensated nonlinearity signals are depicted in the right panels parallel to the left panels of Fig. 16. The four-cycle peak-to-peak periodic nonlinearity can be effectively reduced from 38 pm to 1.2 pm, as shown in Fig. 16d. But 124 pm eight-cycle nonlinearity cannot be reduced (see Fig. 16c).
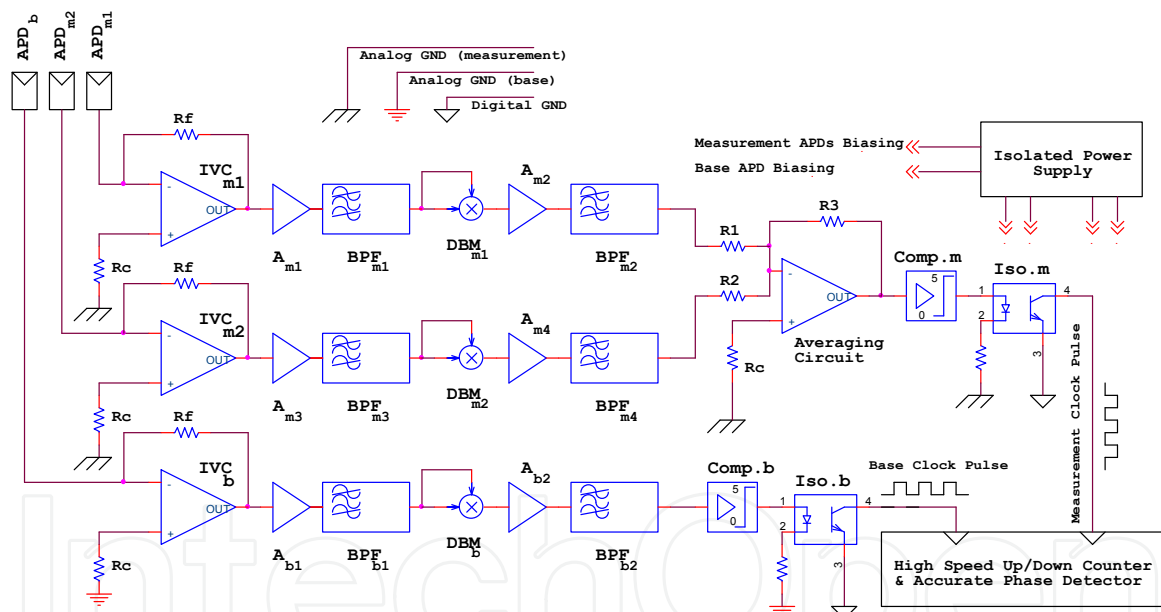

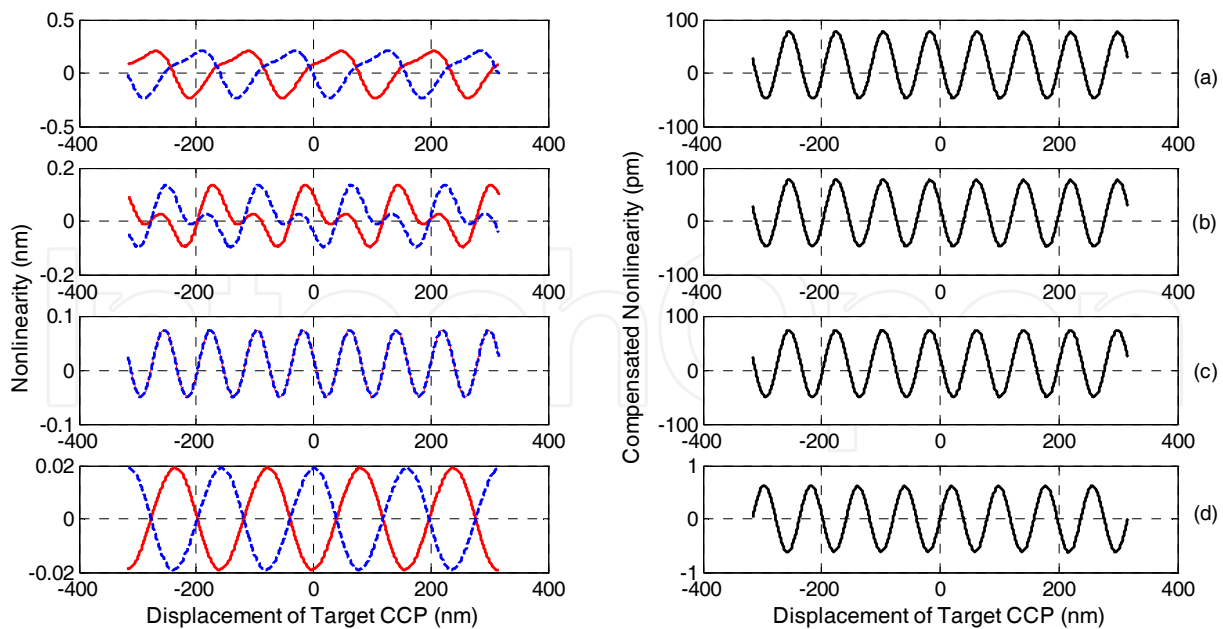Fig. 15. The designed TLMI with noise, nonlinearity and error reduction

Fig. 16. The periodic nonlinearity (left) and compensated nonlinearity (right) in terms of the displacement of target corner cube prism. (a) $\alpha = 2°$, $\delta_{\varepsilon_r} = 0.28°$, $\delta_{\varepsilon_t} = 0.20°$, $\tau_r = 0.95$, $\tau_t = 0.90$, (b) $\alpha = 2°$, $\delta_{\varepsilon_r} = 0.28°$, $\delta_{\varepsilon_t} = 0.20°$, $\rho = 1$, $\tau = 1$, (c) $\alpha = 2°$, $\delta_{\varepsilon_r} = 0.20°$, $\delta_{\varepsilon_t} = 0.20°$, $\rho = 1$, $\tau = 1$ and (d) $\alpha = 0°$, $\delta_{\varepsilon_r} = 0.20°$, $\delta_{\varepsilon_t} = 0.20°$, $\rho = 0.95$, $\tau = 0.90$

5. Conclusion

The optical interferometry is the most frequent technique which has been widely used in metrology systems with sub-nanometer resolution. In this chapter, first we have discussed an overview of principals of interferometry, interfere phenomenon in the laser interferometers and their applications. A comparison of homodyne interferometers, advantages and disadvantages with heterodyne interferometers was also investigated. The optical setup and electronic sections of two- and three-longitudinal-mode heterodyne interferometers was then described. A frequency-path model of the nano-displacement measurement system based on the laser heterodyne interferometers was presented. This model is described by the AC reference, AC interference, DC interference and optical power components of the multi-mode, multi-path interferometer.

The main parameters affecting the displacement measurement accuracy were discussed in the fourth section. The most important errors are related to imperfect alignment of the optical setup and non-ideal polarized modes. The periodic nonlinearity is the principal limitation of the laser interferometers involving polarized light. Therefore, we have analyzed and modelled the periodic nonlinearity resulting from ellipticity and non-orthogonality of the polarised modes, deviation angle and unequal transmission–reflection coefficients of the PBS and a rotation angle of polarizer with two main approaches; plane wave and matrix method based on the Jones calculus. Then by using two polarizers oriented under +45° and -45°, a half-wave plate, and another avalanche photodiode, the periodic nonlinearity has been considerably decreased. In addition it was shown that the first-order nonlinearity can be effectively reduced compared to the second-order nonlinearity.

6. References

Badami, V. G. & Patterson, S. R. (2000). A frequency domain method for the measurement of nonlinearity in heterodyne interferometry. *Precision Eng.*, Vol. 24, 41–49.

Bonsch, G. & Potulski, E. (1998). Measurement of the refractive index of air and comparison with modified Edlen's formula, *Metrologia*, Vol. 35, 133–139.

Brink, M.; Jasper, H.; Slonaker, S.; Wijnhoven, P. & Klaassen, F. (1996). Step-and-scan and step-and-repeat; a technology comparison, Proceeding of SPIE, Vol. 2726, 1996, pp. 734–753.

Cosijns, S. J. A. G. (2004). Displacement laser interferometry with sub-nanometer uncertainty, PhD diss., *Eindhoven Technology Univ.*

Cosijns, S. J. A. G.; Haitjema, H. & Schellekens, P.H. (2002). Modeling and verifying non-linearities in heterodyne displacement interferometry, *Precis. Eng.*, Vol. 26, 448–455.

Demarest, F. C. (1998). High-resolution, high-speed, low data age uncertainty, heterodyne displacement measuring interferometer electronics, *Meas. Sci. Technol.*, Vol. 9, 1024–1030.

Edlen, B. (1966). The refractive index of air, *Metrologia*, Vol. 2, 71–79.

Eom, T. B.; Choi, H.S.; & Lee, S.K. (2002). Frequency stabilization of an internal mirror He–Ne laser by digital control, *Rev. Sci. Instrum.*, Vol. 73, 221–224.

Eom, T. B.; Kim, J.Y, & Jeong, K. (2001). The dynamic compensation of nonlinearity in a homodyne laser interferometer', *Meas. Sci. Technol.*, Vol. 12, 1734–1738.

Freitas, J. M. (1997). Analysis of laser source birefringence and dichroism on nonlinearity in heterodyne interferometry', *Meas. Sci. Technol.*, Vol. 8, 1356–1359.

Hariharan, P. (2003). *Optical interferometry.* USA: Elsevier Science, 9-18, United States of America.

Hou, W. & Zhaox X. (1994). Drift of nonlinearity in the heterodyne interferometer. *Prec. Eng.*, Vol. 16, 25–35.

Hou, W. (2006). Optical parts and the nonlinearity in heterodyne interferometers. *Prec. Eng.*, Vol. 30, 337–346

Hou, W., & Wilkening, G. (1992). Investigation and compensation of the non-linearity of heterodyne interferometers. *Precis. Eng.*, 14, 91–98

Huang, T. L.; Chen, Y. S.; Shy, J. T. & Liu, H. P. (2000) Two-mode frequency stabilization of an internal-mirror 612 nm He–Ne laser, *Proceeding of Proc. Natl. Sci. Counc.*, , Vol. 24, No. 4, 274–278.

ITRS, http://public.itrs.net, (2008) edition metrology, The international roadmap for semiconductors, accessed November 2009.

Kim, M. S. & Kim, S. W. (2002). Two-longitudinal-mode He–Ne laser for heterodyne interferometry of displacement measurement, *Appl. Opt*, Vol. 41, 5938–5942.

Lin, D.; Jiang, H. & Yin, C. (2000). Analysis of nonlinearity in a high resolution grating interferometer. *Opt. Laser Technol.*, Vol. 32, 95–99.

Meyers, J. F.; Lee, J. W., & Schwartz, R. J. (2001). Characterization of measurement error sources in Doppler global velocimetry, *Meas. Sci. Technol.*, Vol. 12, 357–368.

Olyaee, S. & Nejad, S. M. (2007a). Nonlinearity and frequency-path modelling of three-longitudinal-mode nanometric displacement measurement system, *IET Optoelectron.*, Vol. 1, No. 5, 211-220.

Olyaee, S. & Nejad, S. M. (2007b). Design and simulation of velocity and displacement measurement system with sub nanometer uncertainty based on a new stabilized laser Doppler- interferometer. *Arabian J. Sci. Eng*, Vol. 32, 90-99.

Olyaee, S. & Nejad, S. M. (2007c). Error analysis, design and modeling of an improved heterodyne nanodisplacement interferometer, *Iranian Journal of Electrical & Electronic Engineering*, Vol. 3, 53-63

Olyaee, S.; Yoon, T. H. & Hamedi, S. (2009). Jones matrix analysis of frequency mixing error in three-longitudinal-mode laser heterodyne interferometer. *IET Optoelectron.*, Vol. 3, 215–224.

Schattenburg, M. L. & Smith, H. I. (2001). The critical role of metrology in nanotechnology, *Proceeding of SPIE*, Vol. 4608, 116-124.

Schmitz, T. & Beckwith, J. F. (2003). An investigation of two unexplored periodic error sources in differential-path interferometry, *Precis. Eng.*, Vol. 2, 311–322.

Sutton, C. M. (1998). Nonlinearity in the length measurement using heterodyne laser Michelson interferometry. *J. Phys. E: Sci. Instrum.*, 1987, 20, pp. 1290–1292.

Wu, C. (2003). Periodic nonlinearity resulting from ghost reflections in heterodyne interferometry, *Opt. Commun.*, Vol. 215, 17–23.

Wu, C.; Lin, M. S. T.; & Fu, J. (2002). Heterodyne interferometer with two spatial separated polarization beams for nanometrology. *Optical and Quantum Electron.*, Vol. 34, 1267-1276.

Wu, Ch. M. & Su, Ch. Sh. (1996). Nonlinearity in measurements of length by optical interferometry. *Meas. Sci. Technol.*, Vol. **7,** 62–68.

Wu, Ch. M.; Su, Ch. Sh. & Peng, G. Sh. (1996). Correction of nonlinearity in one-frequency optical interferometry, *Meas. Sci. Technol*. Vol. 7, 520–524.

Wuy, C.; & Su, C. (1996). Nonlinearity in measurements of length by optical interferometry, *Meas. Sci. Technol.*, Vol. 7, 62–68.

Yeom, J. Y. & Yoon T. H. (2005). Three-longitudinal-mode He–Ne laser frequency stabilized at 633 nm by thermal phase locking of the secondary beat frequency. *Appl. Opt.*, Vol. 44, 266–270.

Yokoyama, S.; Araki, T. & Suzuki, N. (1994) Intermode beat stabilized laser with frequency pulling, *Appl. Opt*, , Vol. 33, No. 3, 358–363.

Yokoyama, S.; Yokoyama, T. & Araki, T. (2005). High-speed subnanometre interferometry using an improved three-mode heterodyne interferometer, *Meas. Sci. Technol*, Vol. 12, 157–162.

Yokoyama, T.; Araki, T.; Yokoyama, S. & Suzuki, N. (2001). A subnanometre heterodyne interferometric system with improved phase sensitivity using a three-longitudinal-mode He–Ne laser, *Meas. Sci. Technol*,Vol. 12, 157–162.

Advances in Measurement Systems

Edited by Milind Kr Sharma

How to reference

In order to correctly reference this scholarly work, feel free to copy and paste the following:

INTECH
open science | open minds